Multimedia Tools and Applications (2024) 83:3497–3524
https://doi.org/10.1007/s11042-023-15281-5

Multi-classification approach for lung nodule detection and classification with proposed texture feature in X-ray images

Mary Jaya VJ[1] · **Krishnakumar S**[2]

Received: 23 June 2022 / Revised: 22 October 2022 / Accepted: 6 April 2023 /
Published online: 17 May 2023

Abstract

Lung cancer is a widespread type of cancer around the world. It is, moreover, a lethal type of tumor. Nevertheless, analysis signifies that earlier recognition of lung cancer considerably develops the possibilities of survival. By deploying X-rays and Computed Tomography (CT) scans, radiologists could identify hazardous nodules at an earlier period. However, when more citizens adopt these diagnoses, the workload rises for radiologists. Computer Assisted Diagnosis (CAD)-based detection systems can identify these nodules automatically and could assist radiologists in reducing their workloads. However, they result in lower sensitivity and a higher count of false positives. The proposed work introduces a new approach for Lung Nodule (LN) detection. At first, Histogram Equalization (HE) is done during pre-processing. As the next step, improved Balanced Iterative Reducing and Clustering using Hierarchies (BIRCH) based segmentation is done. Then, the characteristics, including "Gray Level Run-Length Matrix (GLRM), Gray Level Co-Occurrence Matrix (GLCM), and the proposed Local Vector Pattern (LVP)," are retrieved. These features are then categorized utilizing an optimized Convolutional Neural Network (CNN) and itdetectsnodule or non-nodule images. Subsequently, Long Short-Term Memory (LSTM) is deployed to categorize nodule types (benign, malignant, or normal). The CNN weights are fine-tuned by the Chaotic Population-based Beetle Swarm Algorithm (CP-BSA). Finally, the superiority of the proposed approach is confirmed across various measures. The developed approach has exhibited a high precision value of 0.9575 for the best case scenario, and high sensitivity value of 0.9646 for the mean case scenario. The superiority of the proposed approach is confirmed across various measures.

Keywords Lung cancer · Improved BIRCH · Proposed LVP features · Optimized CNN · CP-BSA Algorithm

✉ Mary Jaya VJ
jayamary@assumptioncollege.edu.in

Krishnakumar S
drkrishsan@gmail.com

[1] Department of Computer Science, Assumption Autonomous College, Changanassery, Kerala, India

[2] Department of Electronics, School of Technology and Applied Sciences, Mahatma Gandhi University Research Centre, Kochi, Kerala, India

Nomenclature

Abbreviation	Description
AI	Artificial Intelligence
Bi-LSTM	Bidierctional LSTM
BIRCH	Balanced Iterative Reducing and Clustering using Hierarchies
BOA	Butterfly Optimization Algorithm
BSO	Beetle Swarm Optimization
CAD	Computer Assisted Diagnosis
CE	Contrast Enhancement
CNN	Convolutional Neural Network
CT	Computed Tomography
CXR	Chest X-Ray Radiograph
DL	Deep Learning
DNN	Deep Neural Network
FDR	False Discovery Rate
FE	Feature Extraction
FNR	False Negative Rate
FPR	False Positive Rate
GLCM	Gray Level Co-Occurrence Matrix
GLRM	Gray Level Run-Length Matrix
GOT	Geometric Mean-Based Otsu Thresholding
HE	Histogram Equalization
KL	Kullback-Leibler
LA	Lion Algorithm
LDA	Linear Discriminant Analysis
LN	Lung Nodule
LP	Local Pattern
LR	Learning Rate
LSTM	Long Short-Term Memory
LVP	Local Vector Pattern
MCC	Matthews Correlation Coefficient
MC-CLAHE	Modified Clip Limit-Based Contrasts Limited Adaptive Histograms Equalization
ML	Machine Learning
MRCN	Multi-Resolution Convolutional Networks
MU	Mask Unit
NN	Neural Networks
NPV	Negative Predictive Value
PNN	Probabilistic Neural Network
PRO	Poor Rich Optimization
PSO	Particle Swarm Algorithm
RNN	Recurrent Neural Network
ROI	Regions Of Interest
SMO	Spider Monkey Optimization
SSA	Salp Swarm Optimization
SSO	Shark Smell Optimization
SVM	Support Vector Machine
TWEDLNN	Target Based Weighted Elman DL NN
WNLM	White Nodule-Likeness Map

1 Introduction

Lung cancer is said to be a much deadlier disease. It possesses higher casualty rates, and its occurrence rate is rising globally [18, 29, 34, 54]. The last analysis of lung cancer is the main aspect of offering the finest potential clinical cure for patients. Several diseases, like lung cancer, are diagnosed early by routine health screening. As an early diagnostic tool for several medical conditions, an X-ray radiograph is normally deployed for radiological tests in fitness screening by making up almost every examination in a typical radiology sector [16, 26].

Unlike CXR, CT provided 3D data and was deployed for screening for lung cancer [1, 47]. The results demonstrate that low dosage C.T. for screening lung cancer is better than benchmark CXR; however, CT also revealed superior FPR. Based on the current study, the appliance of new CAD software might manipulate the efficacy of CXR. It can eventually be a cost-effective technique in which low-dosage C.T. delivery is not possible due to costs or infrastructure constraints [20, 53]. Conventionally, CXR images are computed by doctors and radiologists. But most hospices endure a deficiency of practicing radiologists [25, 48].

A CAD system assists in the finding of unremarkable lung nodules [6, 12, 43]. Alternatively, in several crowded countries, extreme CXR images must be analyzed in a short period when doing wide-ranging fitness screening. Accordingly, doctors fail to spot certain unremarkable nodules. Earlier research regarding lung nodule recognition employed the differentiation of candidates' shapes under different thresholds because the characteristics recognized nodules from another candidate. However, these schemes only measured the shape and intensity of the lung nodule candidate and thereby couldn't attain high sensitivity and lower FPR simultaneously [38, 46, 51]. Furthermore, in the field of healthcare, deep learning methods are utilized in many applications such as lung nodule classification, COVID-19 medical image processing, and so on [5, 21, 22, 40]. Current research regarding lung nodule recognition including gradient features & texture features for identifying lung nodules from pre-identified candidates.

Major contributions of the research study:

- Introduces an improved BIRCH clustering model for the segmentation process. This is an enhanced form of the traditional BIRCH model.
- For feature extraction, it derives the proposed LVP features along with GLCM & GLRM characteristics.
- Deploys ahybrid optimized CNN classifier and an LSTM classifierfor precise LN detection outputs.
- Introduces a novel CP-BSA scheme for finding the optimal weights in CNN. The proposed CP-BSA model is a modified form of the traditional BSO algorithm.

Organization: Section 2 reviews the study. Section 3 discussesthe suggested LN detection approach. Section 4 depictshybrid classification based lung nodule detection with CP-BSA optimization. Finally, sections 5 and 6 depict the outcome as well as conclusions.

2 Literature review

2.1 Related works

In 2021, Mesut *et al.* [45] introduced AI-based optimization techniques for realizing the categorization of colon and lung cancer his to pathological images. The deployed dataset includes 5 groups of his to pathological images with 3 classes of lung cancer

and 2 classes of colon cancer. In the developed scheme, the DarkNet-19 model was used to train the image groups from scratches and features derived from the DarkNet-19 model. Finally, the proficient features attained were further categorized with the SVM technique.

In 2019, Li *et al.* [19] introduced a DL oriented lung nodule recognition technique. Here, patch-oriented MRCN was employed for extracting the features and 4 diverse fusion techniques were deployed for categorization. This model has better performance as well as was more robust than the formerly described research.

In 2020, Shayan *et al.* [14] introduced 2 techniques, including DNN on fractal image features and CNN techniques with the usage of lung images in a direct manner. Consequently, classification resultants have shown that the offered CNN model outperformed the DNN scheme with higher accurateness and sensitivity. Furthermore, CNN architecture was offered during the segmentation procedure to discover ruined tissue in lung images.

In 2021, Sundhari *et al.* [41] deployed LDA for lung disease recognition. First, the pixel intensity was measured via enhanced HE and integrated with the rib model and original image to improve the initial intensity. Eventually, the rib borders were identified and smoothened with the usage of pixel intensity. The extraction of the white nodule was the subsequent stage. For creating the WNLM, an NN classifier was employed.

In 2018, Marcin *et al.* [52] presented a novel classification technique for lung carcinoma. This technique begins with the extraction as well as localization of LN via evaluating every pixel of the real image. First, in variance images, the local maxima were discovered. By deploying the positions of these maxima in a real image, the shapes of feasible nodules were found in lung tissues. Nevertheless, following this segmentation phase, many false nodules were discovered. As a result, PNN was used as a classifier to differentiate the factual ones.

In 2021, Burkhardt *et al.* [8] evaluated 88 radiographs of both contrasts depending upon mean values for 2 ROI, with healthier left lung and an (irradiated) right lung. In addition, the proportions of mean values were compared among damaged and healthy lungs for contrast. While differences from healthier lungs go beyond 3σ, the time-point was established and evaluated amongst contrasts.

In 2021, Vijay et al. [49] established pre-processing image scheme for alleviating intensity deviations among medicinal images. Then, features like Q-deformed entropy and DL were extracted, and thus, the anomalous marker, lesions and sound impedance from tissues were removed from the images. The obtained qualities were incorporated for differentiating among pneumonia, COVID-19 and healthier cases. The most important intention of this scheme was to generate an image processing device for medicinal experts.

In 2020, Laxmikant *et al.* [44] suggested an efficient DL method for detecting lung cancers by employing TWEDLNN, and MU oriented 3FCM schemes. The established scheme included segmentation of lung image by means of GOT; CE by means of MC-CLAHE; FE; classification by means of TWEDLNN; and MU oriented FCM for detecting LN.

2.2 Motivation

Table 1 represents the reviews of the existing lung nodule detection systems. Some limitations of the extant works are listed below. The main disadvantage of the ANN [45] model was the lack of pre-processing technique to reduce the noise of images. The MRCN was exploited in [19], and it requires implementation on a larger database. The CNN [14] model has to do more with AI methods. Furthermore, more features should be explored in

Table 1 Analysis on existing Lung Nodule detection based schemes

Author	Approach	Advantages	Disadvantages
Mesut *et al.* [45]	ANN	• Good accuracy • Improved sensitivity	• Lack of pre-processing technique to minimize the noise of images.
Xuechen *et al.* [19]	MRCN	• Minimal false positive • High sensitivity	• Need implementation on larger database
Shayan *et al.* [14]	CNN	• Superior accuracy • Improved sensitivity	• Future study was related with AI techniques.
Sundhari *et al.* [41]	WNLM	• Minimal error • Reduced execution time	• More features should be explored
Marcin *et al.* [52]	PNN	• Minimal classification error • High sensitivity	• Fails in detecting lower contrast modules
Burkhardt *et al.* [8]	Wilcoxon-Mann-Whitney test	• High specificity • Better sensitivity	• Decreases dark-field signal
Vijay *et al.* [49]	Q-deformed entropy	• Highly accurate • Improved precision	• Need analysis on complexity
Laxmikant *et al.* [44]	FCM	• Better PSNR • Minimal error	• Need analysis on realistic appliances

the WNLM model [41]. The PNN model [52] fails to detect lower contrast modules. The Wilcoxon-Mann-Whitney test was exploited in [8], and it decreases the dark-field signal. Additionally, the Q-deformed entropy [49] model needs analysis in terms of complexity.

To overcome these limitations, a novel multi-classification approach for LN detection has been introduced. To tackle the limitations of [45], a HE model is utilized for pre-processing. For feature extraction, GLCM, GLRM, and proposed LVP features are extracted rather than the reference [41]. Also, for precise detection, a novel CP-BSA model is deployed for optimally tuning the weights of the CNN classifier.

3 Proposed lung nodule detection approach

Despite the fact that early identification of lung cancer can significantly enhance a lung scanner patient's likelihood of survival, a reliable as well as effective system is critical. The established CP-BSA-based technique is depicted diagrammatically in Fig. 1. The implemented strategy includes the following critical stages. To obtain a segmented lung

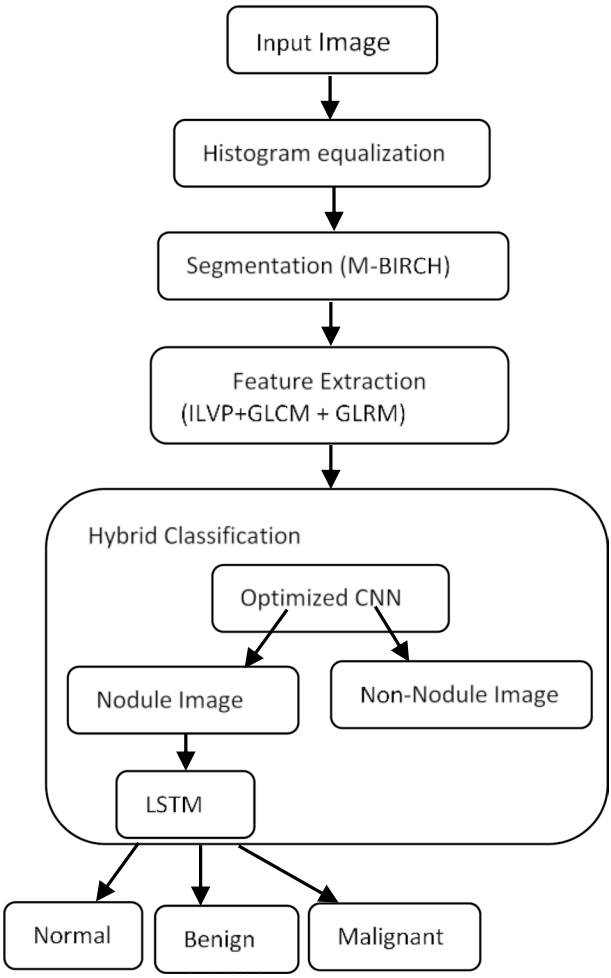

Fig. 1 Suggested Lung Nodule detection scheme architecture

image, HE is utilized throughout pre-processing, followed by improved BIRCH-based segmentation. The features are then derived, including "proposed LVP features, GLCM features, as well as GLRM features". The retrieved characteristics are then fed into an optimized CNN to detect nodule and non-nodule images. The nodule images are then exposed to the LSTM structure to obtain the final output of the nodule type. Particularly, the CNN weights are optimized using the CP-BSA scheme, which aids in achieving better results. Finally, the benefit of the adopted model is confirmed across multiple metrics.

3.1 Pre-processing by histogram equalization

The lung image is initially pre-processed via an HE model, which adjusts the image intensities to enhance contrast. When the image's useful information is depicted by close-contrast values, this strategy often improves the global contrast of numerous photos. With this change, the intensities on the histogram can be more evenly dispersed. As a result, areas with poor local contrast can acquire contrast. This is accomplished through histogram equalization, which effectively spreads out the most frequent intensity values [28].

The attained pre-processed image isindicated by (Im_{HE}).

3.2 Improved BIRCH model for Segmentation

The BIRCH clustering [55] deploys the pixel grey values of the image as sample data and ignores the domain association among the pixels (spatial data). A neighboring pixel is assumed to be in the same class as it is based on the characteristics of medical imaging. To lessen the noise effect on a segmented cluster, a novel image is created using the grey means in a tiny neighborhood of each pixel for medical images. Conventionally, the distance between pixels is computed depend on the difference among the centre & reference pixels. However, as per the developed improved BIRCH model, the distance assessment is performed by KL divergence distance (Di) as shown in Eq. (1), here, ***we*** is the weight, x_i is the centre pixel, y_i and reference pixel n refers to the total count of pixels.

$$Di(x, y) = \sum_{i=1}^{n} \left(x_i - y_i\right) \log \frac{x_i}{y_i} * we \tag{1}$$

The segmented image is represented by Im^{seg}. The pseudo-code of the segmentation scheme is depicted below.

Algorithm 1: Improved BIRCH scheme

Input: pre-processed image (Im_{HE})
Initializethe arrays
for all image pixels
Define the minimum distance between two points
Compute the distance of the pixel based on Eq. (1)
end
Compute centroid
Perform segmentation based on new centroid values

3.3 Feature extraction

In this section, the GLCM, GLRM, and modified LVP features are retrieved from the segmented image.

3.3.1 GLCM features

It is deployed for computing the spatial relationship amongst the pixel [3]. The extracted GLCM features are listed as follows: "entropy, difference variance, contrast, energy, sum variance, correlation, information measures of correlation 1, sum average, homogeneity, variance, sum entropy, MCC(2ndhigher Eigen value of $Q)^{0.5}$, difference entropy, & information measures of correlation 2."The characteristics derived from GLRM are represented as (f_{GLCM}).

3.3.2 GLRM features

"Geometrical features are represented through a matrix in GLRM. It gauges the intensity of the pixels along the designated Run-length direction [27]." The extracted GLRM features are given as follows: "run length non uniformity, grey level non uniformity, small run emphasis, low grey level run emphasis, long run emphasis, high grey level run emphasis, as well asrun percentage." The features derived from GLRM are represented as (f_{GLRM}).

3.3.3 Modified LVP features

The LVP model was introduced for providing different 2-D spatial structures of micro-patterns with a variety of pair wise vector directions of neighborhood pixel and reference pixel. In recent times, LVP is deployed in many extant works to prevail over the disadvantages of other LP descriptors [10]. In this research, it is planned to carry out LVP based on the harmonic mean to attain more accurate features and it is known as proposed LVP. The distance execution is performed by the manhattan distance and the improved LVP is shown in Eq. (2), where, $V_{\alpha}^{Dis}(C)$ denote the derivative vector of C at α direction, Dis denote the manhattan distance as well as C is the reference pixel. Also, $f_4^{Dis}(.)$ it refers to the LVP at a Manhattan-based neighbourhood distance Dis as well as α is the index angle.

$$f_{ILVP} = f_4^{Dis}(C, \alpha) = \sum_{P=1}^{M_P} 2^{P-1} Z_{lvp}^{Dis}(P, C, \alpha) \tag{2}$$

$$Z_{lvp}^{Dis}(P, C, \alpha) = \left\{ \begin{array}{l} 1; \, if \;\; CST_{P,C,\alpha}^{Dis} \geq 0 \\ 0; \, otherwise \end{array} \right\} \tag{3}$$

$$CST_{P,C,\alpha}^{Dis} = V_{\alpha+45^0}^{Dis}(P) - \left[\frac{V_{\alpha+45^0}^{Dis} \Sigma(C)}{V_{\alpha}^{Dis}(C)} \times V_{\alpha}^{Dis}(P) \right] \tag{4}$$

$$V_{\alpha}^{Dis}(C) = \mathrm{Im}(\alpha, Dis) - \mathrm{Im}(C) \tag{5}$$

The retrieved modified LVP based characteristics are denoted as (f_{ILVP}). The pseudocode for modified LVP features is shown in algorithm 2.

Algorithm 2: Modified LVP

Input the segmented image (Im_{seg})
InitializeLVP parameters
Localize the neighborhood pixels
for every centre pixel
Initialize the CST function
for every direction
for each neighbor pixel
Compute the direction based on manhattan based neighborhood distance as in Eq. (2)
Compute harmonic mean
end
Compute the LVP of the pixel
Save the LVP of the pixel at a particular angle
end
Increase pixel index ← next pixel index
end
Extract modified LVP (f_{ILVP})

Accordingly, the derived improved LVP features (f_{ILVP}), GLCM features (f_{GLCM}) and GLRM features (f_{GLRM}) are summed up as *FE* classified via optimized CNN and LSTM classifier for detection.

4 Hybrid classification based LN detection with CP-BSA optimization

4.1 Optimized CNN classifier

CNN's are similar to conventional ANNs in that they are made up of neurons that learn to optimize themselves [9, 13, 37]. Figure 2 depicts the CNN's overall architecture. Due to its benefits, such as high prediction accuracy, weight sharing capability, as well as good computing complexity, CNN is used for classification in this study. Convolutional,

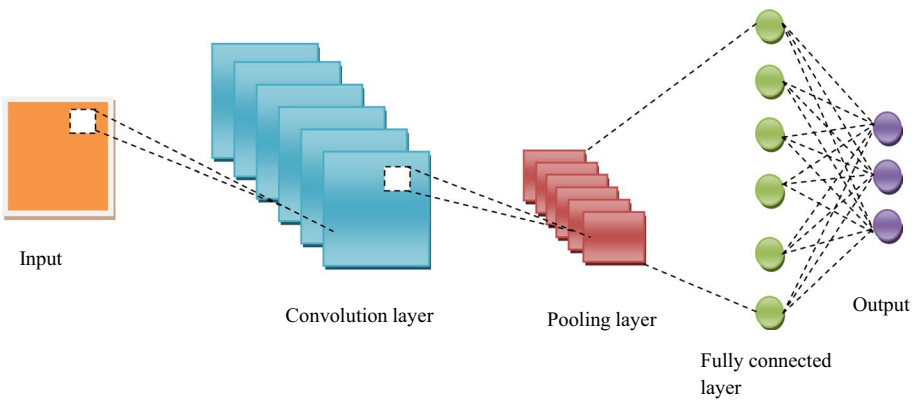

Fig. 2 CNN model

pooling, & fully-connected layers are the three distinct CNN layers. All neurons are connected with adjacent neurons in the last layer.

At a position (r,t) in l^{th} a layer of the related w^{th} feature map, the features are computed as per Eq. (6).

$$B^{l}_{r,t,w} = {W^{l}_{w}}^{T} QI^{l}_{r,t} + T^{l}_{w} \tag{6}$$

In Eq. (6), W^{l}_{w} denote weight optimally tuned deploying theCP-BSA method as well as T^{l}_{w} denote bias term of w^{th} filter connected to l^{th} layer. At a centred layer location, the patch input is denoted by $QI^{l}_{r,t}$. Finally, the activation value $\left(act^{l}_{r,t,w}\right)$ linked to convolutional features $B^{l}_{r,t,w}$is determined as per Eq. (7).

$$act^{l}_{r,t,w} = act\left(B^{l}_{r,t,w}\right) \tag{7}$$

The pooling layer carries down sampling functions achieved from convolutional layers. For each pooling function $\boldsymbol{pool}(\bullet)act^{l}_{m,h,w}$, the $A^{l}_{r,t,w}$ value is evaluated by Eq. (8), here $NN_{r,t}$ denote a neighbourhood near a location (r,t).

$$A^{l}_{r,t,w} = \boldsymbol{pool}\left(act^{l}_{m,h,w}\right), \forall (m.h) \in NN_{r,t} \tag{8}$$

The predictions made by CNN appear in its output layer. As depicted in Eq. (9), the CNN loss is indicated ***Loss***.

$$\boldsymbol{Loss} = \frac{1}{nu}\sum_{h=1}^{nu} l\left(\theta; A^{(h)}; G^{(h)}\right) \tag{9}$$

The elementconnected to W^{l}_{w} and T^{l}_{w} is denoted as θ. Here exist nu counts of output-input relation $\{(QI^{(h)}, A^{(h)}); h \in [1, \cdots, nu]\}$. Also, the h^{th} input feature, the labels, as well as output are indicated as $G^{(h)}$ respectively.

Furthermore, the CNN weights are chosen optimally via the CP-BSA scheme for accurate detection. From CNN output, it can be determined whether the lung image contains a nodule or non-nodule. If the lung image contains nodules, it is further provided as input to LSTM, which provides the final output regarding nodule type (benign, malignant, or normal). For simulation experimentation, 6×1 layer array with layers is utilized, and the details are given in Table 2.

Table 2 CNN layer details

Layer no	Layer name	Description
1	Image Input	15116x1x1 images with 'zerocenter' normalization
2	Convolution	1 1×1 convolutions with stride [1 1] and padding 'same'
3	ReLU	ReLU
4	Fully Connected	2 fully connected layer
5	Softmax	Softmax
6	Classification Output	Crossentropy ex

4.2 LSTM Classifier

The LSTM configuration makes use of a list of repeated LSTM cells. The "forget gate, input gate, and output gate" are represented by the three multiplicative units that make up each LSTM cell [33, 56]. The LSTM memory cells can retain as well as transport information for extended periods of time due to these units. Figure 3 depicts the LSTM's overall architecture.

Consider, hidden and cell states parameters (R & D). At the time, t, the output, input, as well as forget gate imply O_t, I_t, F_t. LSTM is employed F_t for sorting the information to neglect. The sorted information represent particular partial characteristics connected to the past gaze direction, and F_t is defined in accordance with Eq. (10).

$$F_t = \sigma\left(J_{\boldsymbol{IF}} X_t + E_{\boldsymbol{IF}} + J_{RF} R_{t-1} + E_{RF}\right) \tag{10}$$

Eq. (10), (J_{RF}, E_{RF}) & $(J_{\boldsymbol{IF}}, E_{\boldsymbol{IF}})$ stand for weight as well as bias elements to connect hidden & input layers to forget gates, while σ indicates an activation function.

The LSTM uses the input gate as demonstrated in Eqs. (11)–(13), wherein (J_{RG}, E_{RG}) & (J_{IG}, E_{IG}) denote weight & bias constraints to map the hidden & input layers to the cell gate. To map input & hidden layers to I_t, terms (J_{RI}, E_{RI}) & (J_{II}, E_{II}) indicate weight and bias constraints. Layers for input and output are described by (X_t, D_{t-1}, R_{t-1}) & (R_t, D_t).

$$G_t = \tanh\left(J_{IG} X_t + E_{IG} + J_{RG} R_{t-1} + E_{RG}\right) \tag{11}$$

$$I_t = \sigma\left(J_{II} X_t + E_{II} + J_{RI} R_{t-1} + E_{RI}\right) \tag{12}$$

$$D_t = F_t D_{t-1} + I_t G_t \tag{13}$$

Further, the LSTM cell obtains the output hidden layer from the output gate as revealed in Eq. (14) & Eq. (15), here, (J_{RO}, E_{RO}) & (J_{IO}, E_{IO}) implies weight as well as bias to map the hidden & input layer O_t.

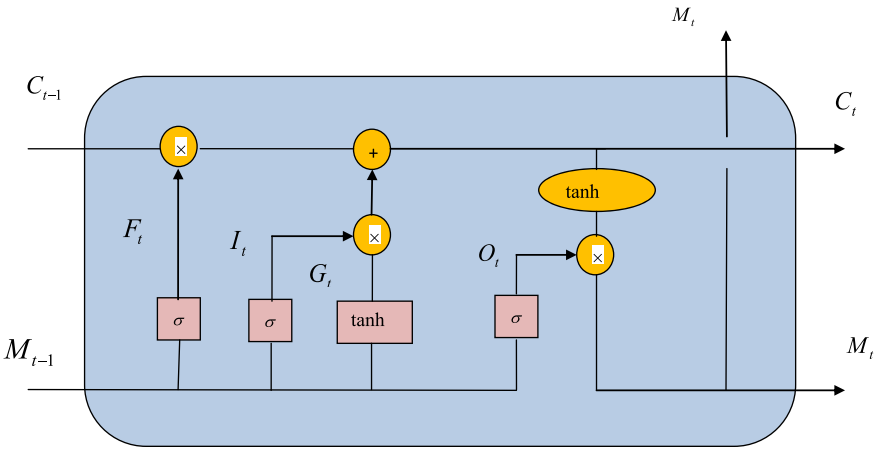

Fig. 3 Architecture of LSTM classifier

Table 3 LSTM layer details

Layer no	Layer name	Description
1	Sequence Input	Sequence input with 15131dimensions
2	LSTM	LSTM with 100 hidden units
3	Fully Connected	3 fully connected layer
4	Softmax	Softmax
5	Classification Output	Crossentropy

$$O_t = \left[\sigma\left(J_{IO}X_t + E_{IO} + J_{RO}R_{t-1} + E_{RO}\right)\right] \tag{14}$$

$$M_t = O_t \tanh\left(D_t\right) \tag{15}$$

Therefore, the output achieved from LSTM gives the final output regarding nodule type(benign, malignant, or normal). For simulation experimentation, 6×1 layer array with layers is utilized, and the details are shown in Table 3.

4.3 Solution encoding

The CNN weights are selected optimally through theCP-BSA model. Solution encoding is depicted in Fig. 4, W_1, W_2, . …, W_{NI} representing the whole number of CNN weights. The objective *Obj* is to minimize the error *Err* as per Eq. (16).

$$Obj = \text{Min}(Er) = \text{Min}(\boldsymbol{Loss}) \tag{16}$$

4.4 CP-BSA algorithm

The BSO is an improved algorithm that incorporates the swarm optimization technique and the beetle foraging process. The current BSO [30] paradigm has several advantages, but there are also some drawbacks. “For instance, the search range for a particle increases as the inertial weights value in the BSO algorithm increases; this indicates a higher global search capacity as well as poorer local search ability. The magnitude of the inertial weight decreases with increasing search range proportional to particle narrow, resulting in a stronger local search capability as well as a weaker global search capability. This study enhances the BSO in order to improve the inertia weight.” Hence, a novelCP-BSA optimization has been developed in this work. Generally, self-enhancement is established to be capable in conventional optimization schemes [11, 15, 30–32, 35, 36, 42, 50].

Fig. 4 Solution encoding

In the established CP-BSA, the beetles share information just like PSO, but their long antennas allow them to be differentiated by the direction and distance they are traveling in.

The mathematical representation of PSO's design was taken. In S-dimensional searching space, there is a population of *NP* beetles denoted as $Y=(Y_1, Y_2, .. Y_{NP})$. The j^{th} beetle indicates an S-dimensional vector $Y_j=(y_{j1}, y_{j2}, .. y_{jS})^T$, denotes the location of the j^{th} beetle, as well as also denotes a potential resolution to the problem. Each beetle position's fitness value is calculated based on the target function. $U_j=(U_{j1}, U_{j2}, .. U_{jS})^T$ represents the beetle j^{th} speed, $M_j=(M_{j1}, M_{j2}, .. M_{jS})^T$ and $M_g=(M_{g1}, M_{g2}, .. M_{gS})^T$ stand for the beetle's individual limit and an excessive population value, respectively. Eq. (17) illustrates the numerical method used to simulate its behavior.

$$Y_{is}^{k+1} = \left(Y_{is}^{k} + \eta U_{is}^{k} + (1-\eta)\zeta_{is}^{k}\right) \tag{17}$$

In Eq. (17), $s=1, 2\ldots S$; $i=1, 2. . NP$; k denotes the current iteration number, U_{is} denotes the beetle speed, ζ_{is} denotes the increase in movement of beetle position as well as η denotes positive constant. Conventionally, speed U is evaluated as per Eq. (18), however, as per introduced CP-BSA model, speed is evaluated based upon chaotic population function. In Eq. (18), φ_1, φ_2 indicates the 2 positive constants, ra_1, ra_2 denotes the 2 arbitrary values between [0, 1], ϖ denotes the inertia weight.

$$U_{is}^{k+1} = \left(\varpi U_{is}^{k} + \varphi_1 ra_1\left(M_{is}^{k} - Y_{is}^{k}\right) + \varphi_2 ra_2\left(M_{gs}^{k} - Y_{gs}^{k}\right)\right) \tag{18}$$

Conventionally, inertia weight is determined as per Eq. (19). As per proposed contribution, a new inertia weight strategy is developed based upon *cos* function as shown in Eq. (20), wherein, *ran* denote the arbitrary integer.

$$\varpi = \varpi_{\max} - \frac{\varpi_{\max} - \varpi_{\min}}{K} * k \tag{19}$$

$$\varpi = \text{ran} * \varpi_{\min} * \left(1 - \cos(h) + \varpi_{\max} * \cos(h)\right) \tag{20}$$

$$h = {}^{\pi K}\Big/_{2k_{\max}} \tag{21}$$

In Eq. (19), $\varpi_{\max}$ & $\varpi_{\min}$ symbolize the maximum as well as minimum value of ϖ. K denotes thelargest iteration number. As ϖ reduces the beetle lessons speed as well asthen, go for local searches.

The term ζ is the incremental function as shown in Eq. (22), which ϑ denotes step size.

$$\zeta_{is}^{k+1} = \vartheta^k U_{is}^{k} * \text{sign}\left(o\left(Y_{rs}^{k}\right) - o\left(Y_{rs}^{k}\right)\right) \tag{22}$$

Eq.(24) correspondingly indicates the searching behaviours of the left as well as right antenna and Eq. (23), which d denote search distance.

$$Y_{rs}^{k+1} = \left(Y_{rs}^{k} + U_{is}^{k} * d/2\right) \tag{23}$$

$$Y_{ls}^{k+1} = \left(Y_{ls}^{k} + U_{is}^{k} * d/2\right) \tag{24}$$

The pseudo-code of the CP-BSA model is presented in Algorithm 3.

Algorithm 3: CP-BSA Model

Initializing swarm $Y_i(i = 1,2...NP)$
Initializing populace speed U
Set ϑ, $\varpi_{min}, \varpi_{max}$, K and pop size
Compute fitness as in Eq. (16)
while $k < K$
  Compute ϖ based on new formula as shown in Eq. (20)
  for every searching agents
    Compute $o(Y_{r2}^k), o(Y_{r2}^k)$ as shown in Eq. (23) and (24)
    ϑ is updated as shown in Eq. (20)
    U is updated based on chaotic population function
    Present search agent position is updated as shown in Eq. (17)
  end for
  Compute fitness as in Eq. (16)
  Record and store the position of every search agent
  for every searching agents
    if $o(y) < o_{pbest}$
      $o_{pbest} = o(y)$
    end if
    if $o(y) < o_{pbest}$
      $o_{gbest} = o(y)$
    end if
  end for
If there is an improved solution, update y^*
ϑ is updated
end while
Return y_{best}, o_{best}

5 Results and discussion

5.1 Experimental setup

The introduced model was executed in **MATLAB**. Consequently, the performance ofnthe introduced approach was measured over extant models such as NN [41], CNN [19], RNN [17], Bi-LSTM [56], SVM [2], HC + BOA [4], HC + SMO [39], HC + PRO [24], and HC + LA [7], HC + SSO [23] and HC + BSO [51] regarding wide-ranging metrics. The experimental performance was executed via changing the learning rate from 60, 70, 80,& 90. The statistical as well as convergence analyses were made to represent the efficacy of the proposed work. Feature analysis and segmentation analysis are also conducted to validate the efficiency of the proposed scheme. During an examination, the training as well as testing rates was set as 70% & 30%.

5.2 Dataset description

For simulation, the investigation was done using a dataset downloaded from the Nodule chest X-ray dataset (https://www.kaggle.com/raddar/nodules-in-chest-xrays-jsrt). The Japanese Society of Radiological Technology (JSRT) provided this dataset, which includes 247 chests X-rays in total. There are 154 that have nodules and 93 that do not have nodules. The images are all 2048 × 2048 pixels in size and have a 12-bit gray scale. Two human observers manually segmented all 154 chest X-ray nodules. Figure 5 shows results of five randomly selected sample images used for segmentation. Figure 5(a) and

(b) are images with nodules and Fig. 5(c) and (d) are non-nodule images. The original image segmented and trained to detect the lung nodules in the original image.

5.3 Performance analysis

The developed HC + CP-BSA outperform existing optimization models hybrid classification using BOA, SMO, PRO, LA, SSO, BSO as well as classification approaches like NN, CNN, RNN, BI-LSTM, and SVM on a variety of measures. Consequently, analysis was held using the dataset in (https://www.kaggle.com/raddar/nodules-in-chest-xrays-jsrt), and Figs. 6, 7 and 8 shows the plot of relevant results. For all the metrics, the presented HC + CP-BSA model has obtained better results than the above mentioned extant

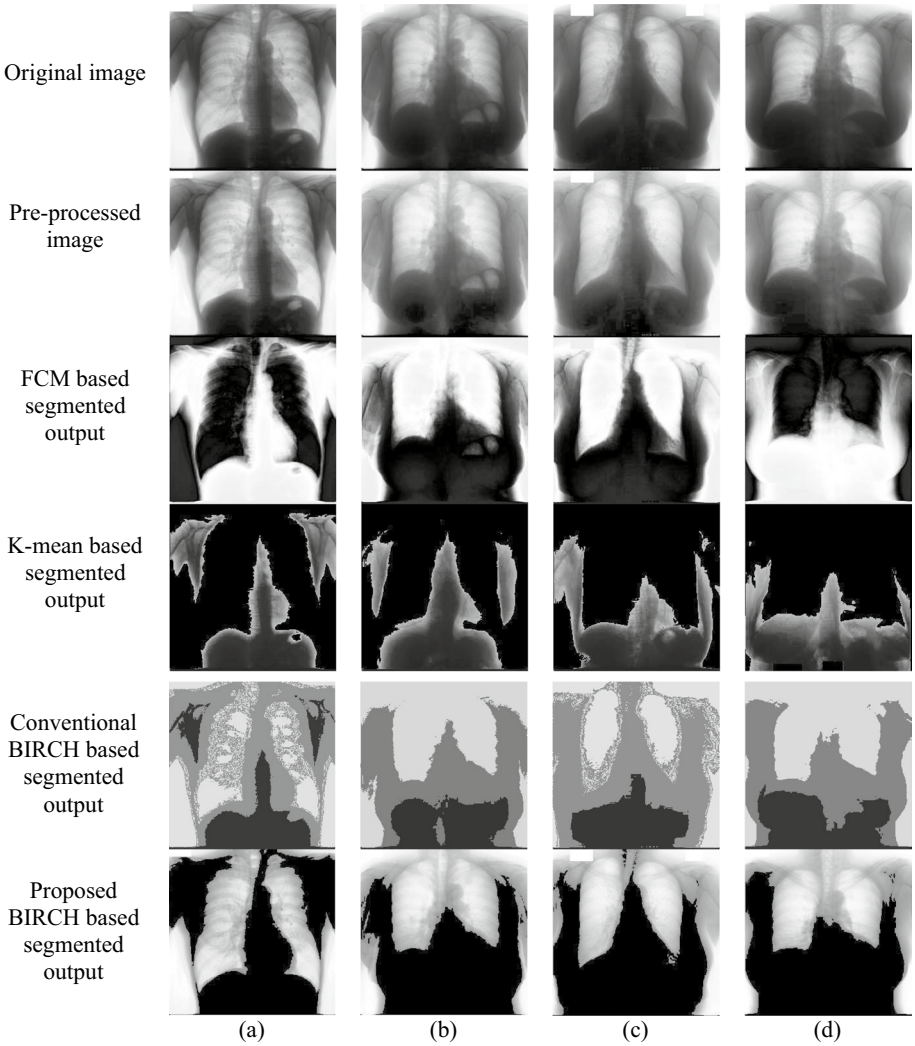

Fig. 5 Sample representation of images for (**a**) nodule 1 (**b**) nodule 2 (**c**) non-nodule 1and (**d**) non-nodule 2

works. In Fig. 6(b), the accuracy of the suggested approach at 90th learning rate is better than other learning rate, i.e. at 90th learning rate; the accuracy of the suggested model is 0.94, whereas, at 70th, the suggested scheme has obtained comparatively lower accuracy values of 0.93. Likewise, for the precision, the outputs for the developed model are increased at 60th learning rate and 90th learning rate. The outputs for sensitivity are high at 60th learning rate and 90th learning rate. The proposed model, the HC + BSO scheme has exposed superior outcomes to the other extant schemes. Thus, from the examination, the effectiveness of the developed HC + CP-BSA is established with the amalgamation of optimization theory.

5.4 Convergence analysis

Figure 9 represents the cost analysis of the suggestedandtraditional models, such as, existing BIRCH + CP-BSA, proposed LVP + CP-BSA, GLCM +CP-BSA, GLRM + CP-BSA, existing LVP + CP-BSA, BOA, SMO, PRO, and L.A., SSO and BSO for varied iterations. Here, the examination changes the iterations from 0, 5, 10, 15, 20, 25,& 30.The suggested CP-BSA has obtained minimum cost values for all iterations than the distinguished schemes mentioned above. Initially, from iteration 0 to iteration 15, the cost values are somewhat superior for adopted and compared models. Here, the suggested LVP + CP-BSA and the existing BIRCH + CP-BSA have both performed poorly in the early versions (0–10). In other words, from iteration 10 to 30, both the compared

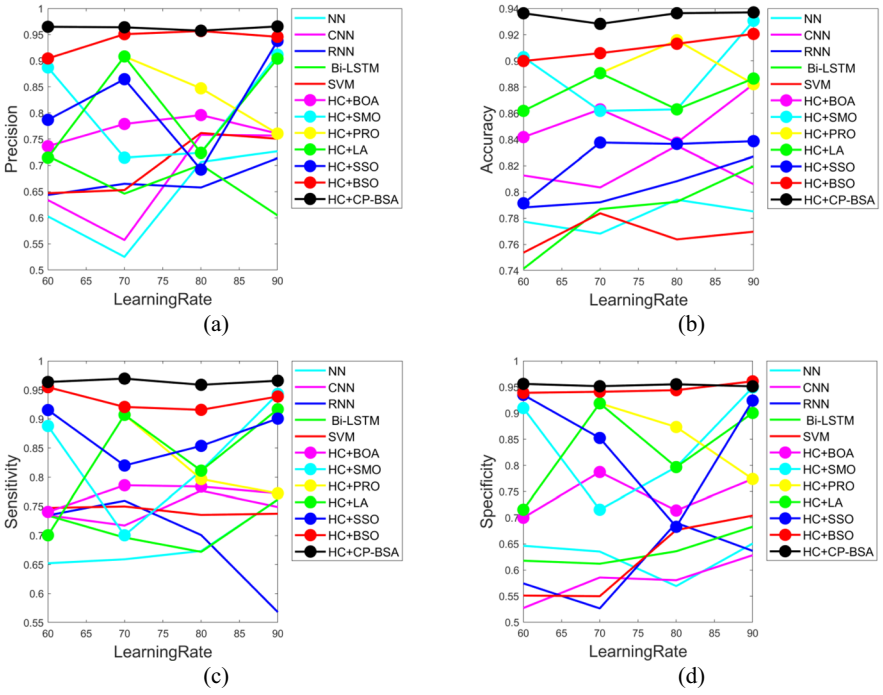

Fig. 6 Analysis employingimplemented&traditionalworksfor"(**a**) precision (**b**) accuracy (**c**) sensitivity & (**d**) specificity"

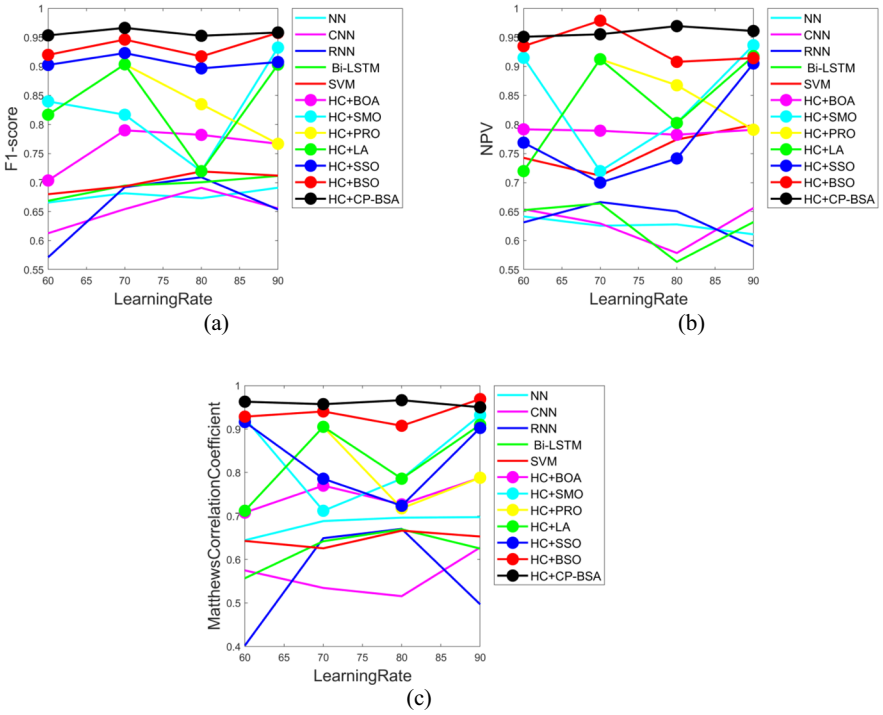

Fig. 7 Analysis employingimplemented&traditional worksfor"(**a**) F1-score (**b**) NPV (**c**) MCC"

and suggested models' cost values continue to decline, but the adopted CP-BSA method yields lower values than the ones that are currently in use. The proposed method has combined the introduced optimization theory to get the least cost value (about 1.05). Thus, the overall assessment supported the progress of the approach that was given. The enhanced model's convergence to the particular fitness is determined.

5.5 Feature analysis

Table 4 depicts the feature analysis of the deployed HC + CP-BSA and the suggested LVP + CP-BSA, GLCM + CP-BSA, GLRM + CP-BSA, the suggested work with existing BIRCH based segmentation, extant LVP based characteristics, as well as proposed model without optimization. Analysis is carried out for a variety of indicators, including FPR, accuracy, etc. The recommended HC + CP-BSA has achieved the highest values when compared to the proposed LVP + CP-BSA, GLCM +CP-BSA, GLRM +CP-BSA, proposed model with existing BIRCH based segmentation, existing LVP based features, and proposed model without optimization. For practically every metric, the results of the current BIRCH-based segmentation have been poorer than those of alternative analyses. This guarantees that the generated model will improve as a result of adopting the CP-BSA hypothesis.

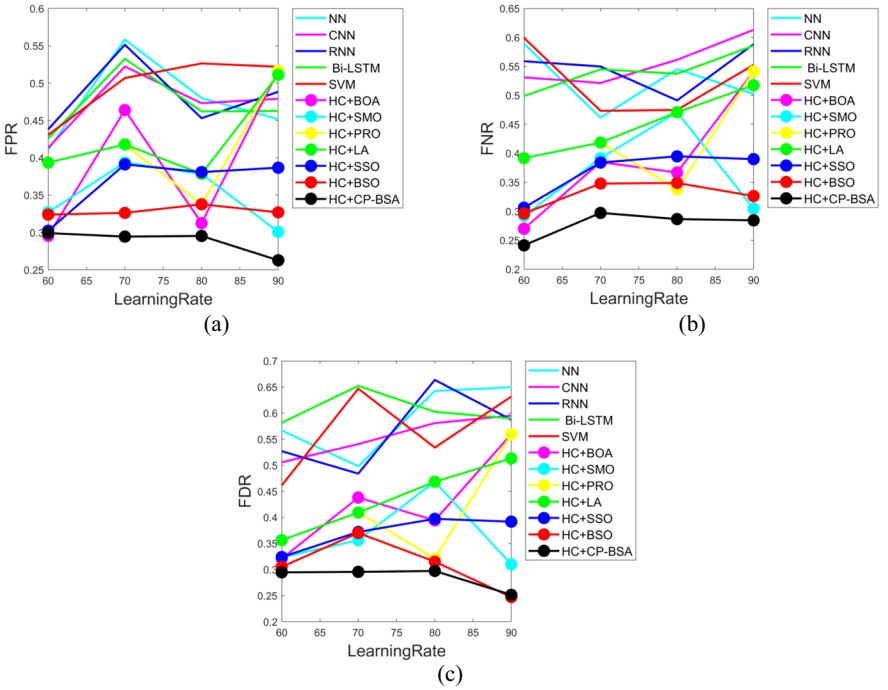

Fig. 8 Analysis employingimplemented&traditional worksfor"(**a**) FPR (**b**) FNR (**c**) FDR"

Fig. 9 Convergence analysis

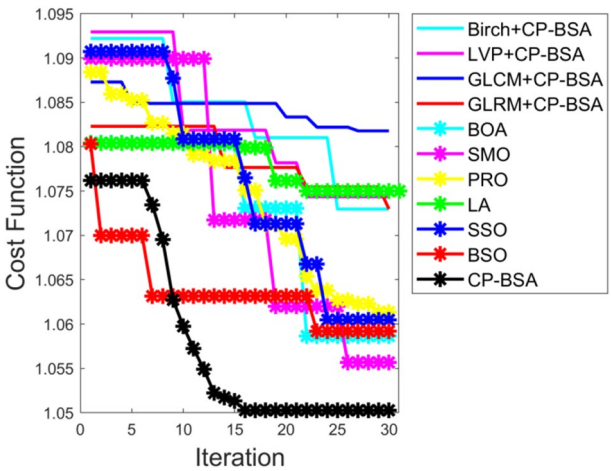

Table 4 Analysis on extant features and optimization theory

Metrics	Proposed LVP+CP-BSA	GLRM+CP-BSA	GLCM- CP-BSA	Existing BIRCH segmentation with CP_BSA	Existing LVP features with CP-BSA	Proposed LVP+GLRM+GLCM without CP_BSA	ProposedHC + CP-BSA
Precision	0.7828	0.7828	0.8209	0.5099	0.5978	0.6968	0.9640
Accuracy	0.7878	0.7603	0.8072	0.7102	0.7564	0.8291	0.9283
Specificity	0.8544	0.8471	0.8779	0.7393	0.7800	0.8338	0.9515
MCC	0.5635	0.5163	0.6070	0.3595	0.4669	0.6283	0.9573
FPR	0.1456	0.1529	0.1221	0.2607	0.2200	0.1662	0.2945
F1-score	0.7385	0.7143	0.7653	0.5681	0.6472	0.7530	0.9663
Sensitivity	0.6990	0.6568	0.7168	0.6413	0.7056	0.8189	0.9696
FDR	0.2172	0.2172	0.1791	0.4901	0.4022	0.3032	0.2956
FNR	0.3010	0.3432	0.2833	0.3588	0.2944	0.1811	0.2972
NPV	0.8544	0.8471	0.8779	0.7393	0.7800	0.8338	0.9554

Table 5 Statistical analysis

Accuracy					
Methods	Mean	Best	Std dev	Worst	Median
NN	0.7813	0.7682	0.0110	0.7942	0.7813
CNN	0.8144	0.8035	0.0144	0.8352	0.8093
RNN	0.8040	0.7882	0.0177	0.8270	0.8003
Bi-LSTM	0.7852	0.7414	0.0325	0.8197	0.7898
SVM	0.7678	0.7537	0.0126	0.7838	0.7668
HC + BOA	0.8561	0.8375	0.0207	0.8822	0.8524
HC + SMO	0.8896	0.8618	0.0334	0.9307	0.8829
HC + PRO	0.8876	0.8618	0.0224	0.9158	0.8864
HC + LA	0.8755	0.8618	0.0152	0.8907	0.8747
HC + SSO	0.8261	0.7914	0.0231	0.8387	0.8371
HC + BSO	0.9099	0.8999	0.0090	0.9206	0.9095
HC + CP-BSA	0.9346	0.9283	0.0042	0.9371	0.9364
Sensitivity					
Methods	Mean	Best	Std dev	Worst	Median
NN	0.6865	0.6522	0.0507	0.7613	0.6662
CNN	0.7444	0.7171	0.0252	0.7768	0.7418
RNN	0.6908	0.5683	0.0852	0.7597	0.7177
Bi-LSTM	0.7161	0.6718	0.0399	0.7619	0.7154
SVM	0.7426	0.7354	0.0072	0.7499	0.7424
HC + BOA	0.7707	0.7406	0.0210	0.7860	0.7781
HC + SMO	0.8357	0.7004	0.1052	0.9432	0.8495
HC + PRO	0.7941	0.7004	0.0857	0.9072	0.7845
HC + LA	0.8339	0.7004	0.1010	0.9169	0.8591
HC + SSO	0.8725	0.8200	0.0438	0.9155	0.8772
HC + BSO	0.9326	0.9158	0.0178	0.9548	0.9298
HC + CP-BSA	0.9646	0.9589	0.0044	0.9696	0.9649
Specificity					
Methods	Mean	Best	Std dev	Worst	Median
NN	0.6254	0.5692	0.0380	0.6507	0.6409
CNN	0.5804	0.5272	0.0415	0.6284	0.5831
RNN	0.6069	0.5264	0.0716	0.6903	0.6055
Bi-LSTM	0.6372	0.6120	0.0321	0.6829	0.6269
SVM	0.6204	0.5498	0.0816	0.7041	0.6138
HC + BOA	0.7438	0.7001	0.0432	0.7872	0.7439
HC + SMO	0.8427	0.7154	0.1067	0.9492	0.8532
HC + PRO	0.8204	0.7154	0.0925	0.9187	0.8236
HC + LA	0.8328	0.7154	0.0949	0.9187	0.8484
HC + SSO	0.8485	0.6827	0.1164	0.9350	0.8881
HC + BSO	0.9462	0.9389	0.0101	0.9609	0.9424
HC + CP-BSA	0.9535	0.9513	0.0025	0.9561	0.9534
Precision					
Methods	Mean	Best	Std dev	Worst	Median
NN	0.6403	0.5251	0.0941	0.7268	0.6546
CNN	0.6765	0.5574	0.0985	0.7583	0.6952
RNN	0.6701	0.6436	0.0305	0.7138	0.6614

Table 5 (continued)

Bi-LSTM	0.6675	0.6045	0.0520	0.7179	0.6737
SVM	0.7030	0.6470	0.0615	0.7616	0.7018
HC + BOA	0.7679	0.7364	0.0255	0.7959	0.7697
HC + SMO	0.8093	0.7147	0.1045	0.9115	0.8055
HC + PRO	0.8076	0.7147	0.0866	0.9081	0.8039
HC + LA	0.8127	0.7147	0.1079	0.9081	0.8139
HC + SSO	0.8204	0.6922	0.1054	0.9379	0.8258
HC + BSO	0.9394	0.9043	0.0238	0.9568	0.9483
HC + CP-BSA	0.9630	0.9575	0.0037	0.9657	0.9645
FPR					
Methods	Mean	Best	Std dev	Worst	Median
NN	0.4753	0.4109	0.0623	0.5585	0.4659
CNN	0.4720	0.4134	0.0448	0.5223	0.4761
RNN	0.4828	0.4382	0.0504	0.5515	0.4708
Bi-LSTM	0.4709	0.4260	0.0446	0.5327	0.4625
SVM	0.4965	0.4308	0.0446	0.5264	0.5144
HC + BOA	0.3972	0.2955	0.1100	0.5167	0.3883
HC + SMO	0.3501	0.3008	0.0435	0.3937	0.3529
HC + PRO	0.4166	0.3380	0.0747	0.5167	0.4058
HC + LA	0.4254	0.3786	0.0595	0.5113	0.4058
HC + SSO	0.3654	0.3024	0.0422	0.3913	0.3839
HC + BSO	0.3288	0.3240	0.0062	0.3378	0.3267
HC + CP-BSA	0.2880	0.2628	0.0169	0.2993	0.2950
F1-score					
Methods	Mean	Best	Std dev	Worst	Median
NN	0.6779	0.6656	0.0110	0.6911	0.6773
CNN	0.6534	0.6128	0.0319	0.6908	0.6550
RNN	0.6566	0.5714	0.0614	0.7092	0.6729
Bi-LSTM	0.6939	0.6686	0.0182	0.7115	0.6976
SVM	0.7012	0.6800	0.0177	0.7191	0.7028
HC + BOA	0.7606	0.7037	0.0392	0.7900	0.7744
HC + SMO	0.8271	0.7196	0.0874	0.9324	0.8283
HC + PRO	0.8305	0.7668	0.0566	0.9036	0.8259
HC + LA	0.8358	0.7196	0.0876	0.9036	0.8600
HC + SSO	0.9074	0.8966	0.0113	0.9230	0.9051
HC + BSO	0.9353	0.9172	0.01991	0.9578	0.9331
HC + CP-BSA	0.9577	0.9527	0.0063	0.9663	0.9559
MCC					
Methods	Mean	Best	Std dev	Worst	Median
NN	0.6817	0.6444	0.0253	0.6976	0.6924
CNN	0.5633	0.5158	0.0495	0.6277	0.5549
RNN	0.5547	0.4022	0.1277	0.6705	0.5731
Bi-LSTM	0.6235	0.5569	0.0479	0.6695	0.6337
SVM	0.6470	0.6259	0.0171	0.6664	0.6478
HC + BOA	0.7482	0.7080	0.0371	0.7881	0.7484
HC + SMO	0.8387	0.7121	0.1079	0.9320	0.8553
HC + PRO	0.7808	0.7121	0.0898	0.9052	0.7529

Table 5 (continued)

HC + LA	0.8283	0.7121	0.0964	0.9099	0.8455
HC + SSO	0.8320	0.7236	0.0931	0.9162	0.8442
HC + BSO	0.9364	0.9075	0.0256	0.9689	0.9345
HC + CP-BSA	0.9591	0.9500	0.0071	0.9663	0.9601
FNR					
Methods	Mean	Best	Std dev	Worst	Median
NN	0.5246	0.4616	0.0548	0.5889	0.5239
CNN	0.5567	0.5214	0.0412	0.6131	0.5462
RNN	0.5471	0.4914	0.0407	0.5884	0.5544
Bi-LSTM	0.5417	0.4989	0.0356	0.5857	0.5412
SVM	0.5250	0.4734	0.0617	0.5991	0.5138
HC + BOA	0.3908	0.2699	0.1124	0.5414	0.3759
HC + SMO	0.3649	0.2922	0.0835	0.4710	0.3482
HC + PRO	0.4225	0.3380	0.0861	0.5414	0.4052
HC + LA	0.4497	0.3918	0.0559	0.5175	0.4448
HC + SSO	0.3688	0.3063	0.0419	0.3948	0.3871
HC + BSO	0.3299	0.2962	0.0247	0.3489	0.3371
HC + CP-BSA	0.2774	0.2413	0.0247	0.2972	0.2855
NPV					
Methods	Mean	Best	Std dev	Worst	Median
NN	0.6265	0.6108	0.0126	0.6416	0.6268
CNN	0.6297	0.5787	0.0360	0.6562	0.6418
RNN	0.6347	0.5902	0.0329	0.6664	0.6410
Bi-LSTM	0.6280	0.5635	0.0450	0.6640	0.6423
SVM	0.7570	0.7119	0.0379	0.7992	0.7583
HC + BOA	0.7886	0.7823	0.0043	0.7917	0.7902
HC + SMO	0.8435	0.7197	0.1012	0.9366	0.8588
HC + PRO	0.8227	0.7197	0.0850	0.9124	0.8293
HC + LA	0.8381	0.7197	0.0951	0.9177	0.8575
HC + SSO	0.7788	0.6999	0.0888	0.9051	0.7551
HC + BSO	0.9340	0.9079	0.0320	0.9788	0.9246
HC + CP-BSA	0.9592	0.9510	0.0080	0.9694	0.9582
FDR					
Methods	Mean	Best	Std dev	Worst	Median
NN	0.6496	0.4981	0.0714	0.5892	0.6046
CNN	0.5952	0.5057	0.0405	0.5556	0.5607
RNN	0.6636	0.4840	0.0780	0.5654	0.5571
Bi-LSTM	0.6522	0.5815	0.0317	0.6065	0.5961
SVM	0.6468	0.4613	0.0872	0.5685	0.5828
HC + BOA	0.5597	0.3208	0.1001	0.4282	0.4162
HC + SMO	0.4684	0.3100	0.0720	0.3645	0.3399
HC + PRO	0.5597	0.3209	0.1052	0.4116	0.3829
HC + LA	0.5132	0.3565	0.0684	0.4368	0.4389
HC + SSO	0.3973	0.3240	0.0333	0.3713	0.3820
HC + BSO	0.3702	0.2473	0.0503	0.3095	0.3102
HC + CP-BSA	0.2974	0.2515	0.0222	0.2848	0.2952

Table 6 Analysis on proposed segmentation model over existing segmentation model

	Improved Birch	Conventional Birch	K-means	FCM
Dice	0.8916	0.8093	0.6086	0.7618
Jaccard	0.8084	0.6942	0.4523	0.6836

5.6 Statistical analysis

The statistical analysis of different measures for the implemented HC+ CP-BSA and traditional models NN, CNN, RNN, Bi-LSTM and SVM as well as hybrid classification employing BOA, SMO, PRO, LA, SSO and BSO are shown in Table 5. The meta-heuristic approaches are stochastic, as well as each model is looked at multiple times to get to Eq. (16) in order to ensure fair estimation. After carefully examining the experimental outcomes, the implemented HC+ CP-BSA method has reached appropriate values for each circumstance.In Table 5, the developed scheme has accomplished better values for positive metrics and the least value for negative metrics. Specifically, the developed approach has exhibited better precision outcomes for all cases. Mainly, a high precision value of 0.9646 is attained for the best case scenario, and high sensitivity value of 0.96457is attained for the mean case scenario.

5.7 Segmentation analysis

Dice and Jaccard metrics are used to compute the accuracy of segmentation. Table 6 describes average value of the segmentation analysis in terms of Dice and Jaccard metrics for improved Birch scheme over conventional schemes. Analysis on proposed Segmentation model over existing Segmentation model for 10 randomly selected individual images is represented in Table 7. While noting the results, the improved Birch has shown enhanced accuracy values than the conventional Birch, K-means and FCM schemes.

Table 7 Analysis on proposed segmentation model over existing segmentation model for 10 individual images

Image	Improved Birch		Convolutional Birch		K-means		FCM	
	Dice	Jaccard	Dice	Jaccard	Dice	Jaccard	Dice	Jaccard
1	0.8717	0.7726	0.8391	0.7228	0.6868	0.5229	0.1965	0.1090
2	0.8787	0.7837	0.8253	0.7025	0.4181	0.2643	0.8879	0.7985
3	0.9853	0.9711	0.5921	0.4206	0.7712	0.6276	0.9870	0.9744
4	0.8319	0.7122	0.9365	0.8805	0.7100	0.5504	0.8522	0.7425
5	0.8903	0.8024	0.8536	0.7445	0.4569	0.2961	0.8851	0.7938
6	0.8257	0.7032	0.9303	0.8696	0.5173	0.3489	0.8448	0.7313
7	0.8736	0.7757	0.8431	0.7287	0.6904	0.5272	0.8894	0.8008
8	0.9331	0.8745	0.7760	0.6340	0.7731	0.6301	0.9334	0.8750
9	0.8144	0.6869	0.9353	0.8784	0.7095	0.5498	0.8324	0.7129
10	0.9188	0.8498	0.8297	0.7089	0.6929	0.5301	0.9149	0.8431

Table 8 Ablation study analysis of the adopted scheme regarding pre-processing technique

LR=60		
Metrics	Without pre-processing+ CP-BSA	With pre-processing+ CP-BSA
Precision	0.5188	0.9650
Accuracy	0.8172	0.9364
Specificity	0.7723	0.9561
Sensitivity	0.7360	0.9639
FPR	0.3160	0.2993
F1-score	0.6832	0.9535
MCC	0.6330	0.9630
FNR	0.2640	0.2413
NPV	0.7723	0.9510
FDR	0.4812	0.2947
LR=70		
Metrics	Without pre-processing+ CP-BSA	With pre- processing+ CP-BSA
Precision	0.6075	0.9640
Accuracy	0.8509	0.9283
Specificity	0.8062	0.9515
Sensitivity	0.6530	0.9696
FPR	0.4671	0.2945
F1-score	0.7558	0.9663
MCC	0.6998	0.9573
FNR	0.3470	0.2972
NPV	0.8062	0.9554
FDR	0.3925	0.2956
LR=80		
Metrics	Without pre-processing+ CP-BSA	With pre- processing+ CP-BSA
Precision	0.5255	0.9575
Accuracy	0.8196	0.9365
Specificity	0.7746	0.9553
Sensitivity	0.6910	0.9589
FPR	0.3481	0.2954
F1-score	0.6890	0.9527
MCC	0.6380	0.9663
FNR	0.3091	0.2866
NPV	0.7746	0.9694
FDR	0.4745	0.2974
LR=90		
Metrics	Without pre-processing+ CP-BSA	With pre- processing+ CP-BSA
Precision	0.5875	0.9657
Accuracy	0.8436	0.9371
Specificity	0.7988	0.9513
Sensitivity	0.6309	0.9660
FPR	0.4268	0.2628
F1-score	0.7402	0.9584
MCC	0.6851	0.9500
FNR	0.3691	0.2844
NPV	0.7988	0.9610
FDR	0.4125	0.2515

Table 9 Computational time analysis

Approaches	Computation time (s)
BSO [51]	165.29
SSO [23]	288.14
LA [7]	176.59
PRO [24]	455.28
SMO [39]	262.66
BOA [4]	178.18
CP-BSA	111.98

5.8 Ablation study analysis

In this research, histogram equalization is utilized for pre-processing and this ablation analysis is evaluated with respect to pre-processing technique. Also, this analysis is performed based on learning rates such as 60, 70, 80, and 90 and shown in Table 8. For learning rate of 60, the accuracy of the propose CP-BSA model without pre-processing is 0.8172 and with pre-processing technique is 0.9364. Also, the precision of the propose CP-BSA model without pre-processing is 0.51878and with pre-processing technique is 0.96495. Similarly, the proposed model withpre-processing technique value is better than the one without pre-processing technique in all LRs. Hence, the superiority of the adopted scheme is proven based on pre-processing technique used.

5.9 Computational time analysis

The computational time of the implemented and traditional models are shown in Table 9. The computation time of the implemented CP-BSA scheme is 111.98 as well as it is 32.25%, 61.14%, 36.59%, 75.4%, 57.37%, and 37.15% better than the extant BSO, SSO, LA, PRO, SMO, and BOA methods respectively. As a result, the robustness of the implemented lung nodule detection work is validated successfully.

6 Conclusion

A unique hybrid classifier-based LN detection model has been created in this paper. Pre-processing was done initially using HE model, and later improved BIRCH-based segmentation was carried out. Then other enhanced features were generated, including "proposed LVP features, GLCM features, and GLRM features". When detecting nodule or non-nodule images, optimal CNN was used to classify these features. Later, LSTM was used to categorize more nodule kinds (benign, malignant, or normal). A new CP-BSA technique is deployed to optimize CNN's weights. In the end, the offered scheme's dominance over the traditional schemes relating to numerous measures was proven. Especially, at 90th learning rate, the sensitivity of proposed model was 20.62%, 22.68%, 41.24%, 22.68%, 23.71%, 20.62%, 2.06%, 20.62%, 5.15%, 7.22%, and 2.06% better than the conventional NN, CNN, RNN, BI-LSTM, and SVM, as well as with hybrid model employing BOA, SMO, PRO, LA, SSO, and BSO approaches respectively. Also, subsequent to proposed model, the HC + BSO scheme has exposed superior outcomes than

the other extant schemes. Hence, the superiority of the suggested work is validated successfully. However, a limited dataset is being utilized and the developed method is limited in capturing the contextual information between slices. In future, it is planned to perform the concerned approach with a 3D CNN model using a larger database.

Acknowledgments I want to thank everyone who has helped me complete this project successfully. I sincerely thank my colleagues for their assistance.

Funding There was no specific funding for this study.

Data availability In support of this study, no new data were generated or analyzed.

Declarations

Conflict of Interest The authors declare that they have no conflicts of interest.

References

1. Alahmari SS, Cherezov D, Goldgof DB, Hall LO, Gillies RJ, Schabath MB (2018) Delta Radiomics Improves Pulmonary Nodule Malignancy Prediction in Lung Cancer Screening. IEEE Access 6:77796–77806
2. Almansour NA, Syed HF, Khayat NR, Altheeb RK, Olatunji SO (2019) Neural network and support vector machine for the prediction of chronic kidney disease: A comparative study. Comput Biol Med 109:101–111
3. Arabi PM, Joshi G, Vamsha Deepa N (2016) Performance evaluation of GLCM and pixel intensity matrix for skin texture analysis. Perspect Sci 8:203–206
4. Arora S, Singh S (2019) Butterfly optimization algorithm: a novel approach for global optimization. Soft Comput 23:715–734. https://doi.org/10.1007/s00500-018-3102-4
5. Bhattacharya S, Maddikunta PKR, Pham Q-V, Gadekallu TR, Chowdhary CL, Alazab M, Piran MJ (2021) Deep learning and medical image processing for coronavirus (COVID-19) pandemic: A survey. Sustain Cities Soc 65:102589
6. Bonavita I, Rafael-Palou X, Ceresa M, Piella G, González Ballester MA (2020) Integration of convolutional neural networks for pulmonary nodule malignancy assessment in a lung cancer classification pipeline. Comput Methods Prog Biomed 185:105172
7. Boothalingam R (2018) Optimization using lion algorithm: a biological inspiration from lion's social behavior. Evol Intel 11:31–52
8. Burkhardt R, Gora T, Fingerle AA et al (2021) Early detection of radiation-induced lung damage with X-ray dark-field radiography in mice. Eur Radiol 31:4175–4183. https://doi.org/10.1007/s00330-020-07459-4
9. Chandanapalli SB, Reddy ES, Lakshmi DR (2019) Convolutional Neural Network for Water Quality Prediction in WSN. J Netw Commun Syst 2(3):40–47
10. Fan KC, Hung TY (2014) A novel local pattern descriptor—local vector pattern in high-order derivative space for face recognition. IEEE Trans Image Process 23:2877–2891
11. George A, Rajakumar BR (2013) APOGA: An Adaptive Population Pool Size based Genetic Algorithm. AASRI Procedia - 2013 AASRI Conference on Intelligent Systems and Control (ISC 2013), Vol. 4, pages: 288–296, https://doi.org/10.1016/j.aasri.2013.10.043
12. Gong J, Liu J-y, Wang L-j, Zheng B, Nie S-d (2016) Computer-aided detection of pulmonary nodules using dynamic self-adaptive template matching and a FLDA classifier. Physica Medica 32(12):1502–1509
13. Gu J, Wang Z, Kuen J, Ma L, Shahroudy A, Shuai B, Liu T, Wang X, Wang G, Cai J, Chen T (2018) Recent advances in convolutional neural networks. Pattern Recogn 77:354–377
14. Hassantabar S, Ahmadi M, Sharifi A (2020) Diagnosis and detection of infected tissue of COVID-19 patients based on lung x-ray image using convolutional neural network approaches. Chaos, Solitons Fractals 140:110170 (Cover date: November 2020)
15. Jadhav AN, Gomathi N (2019) DIGWO: Hybridization of Dragonfly Algorithm with Improved Grey Wolf Optimization Algorithm for Data Clustering. Multimed Res 2(3):1–11

16. Jiang J et al (2019) Multiple Resolution Residually Connected Feature Streams for Automatic Lung Tumor Segmentation From CT Images. IEEE Trans Med Imaging 38(1):134–144
17. Kao L-J, Chiu CC (2020) Application of integrated recurrent neural network with multivariate adaptive regression splines on SPC-EPC process. J Manuf Syst 57:109–118
18. Li K, Chen Y, Sun R et al (2020) Exploring potential of different X-ray imaging methods for early-stage lung cancer detection. Radiat Detect Technol Methods 4:213–221. https://doi.org/10.1007/s41605-020-00173-1
19. Li X, Shen L, Xie X, Huang S, Yu J (2020) Multi-resolution convolutional networks for chest X-ray radiograph based lung nodule detection. Artif Intell Med 103:101744 In press, corrected proof, Available online 28 October 2019
20. Liu H, Cao H, Song E, Ma G, Hung C-C (2019) A cascaded dual-pathway residual network for lung nodule segmentation in C.T. images. Physica Medica 63:112–121
21. Liu X, Song L, Liu S, Zhang Y (2021) A review of deep-learning-based medical image segmentation methods. Sustainability 13(3):1224
22. Liu X, He J, Song L, Liu S, Srivastava G (2021) Medical Image Classification based on an Adaptive Size Deep Learning Model. ACM Trans Multimed Comput Commun Appl (TOMM) 17(3s):1–18
23. Mohammad-Azari S, Bozorg-Haddad O, Chu X (2018) Shark Smell Optimization (SSO) Algorithm. In: Bozorg-Haddad O (ed) Advanced Optimization by Nature-Inspired Algorithms. Studies in Computational Intelligence, vol 720. Springer, Singapore. https://doi.org/10.1007/978-981-10-5221-7_10
24. Moosavi S, Bardsiri V (2019) Poor and rich optimization algorithm: A new human-based and multi populations algorithm. Eng Appl Artif Intell 86:165–181. https://doi.org/10.1016/j.engappai.2019.08.025
25. Nomura Y, Higaki T, Fujita M, Miki S, Awai K (2017) Effects of Iterative Reconstruction Algorithms on Computer-assisted Detection (CAD) Software for Lung Nodules in Ultra-low-dose CT for Lung Cancer Screening. Acad Radiol 24(2):124–130
26. Petousis P, Winter A, Speier W, Aberle DR, Hsu W, Bui AAT (2019) Using Sequential Decision Making to Improve Lung Cancer Screening Performance. IEEE Access 7:119403–119419
27. Radhakrishnan M, Kuttiannan T (2012) Comparative Analysis of Feature Extraction Methods for the Classification of Prostate Cancer from TRUS Medical Images. IJCSI Int J Comput Sci Issues 9(1):171–179
28. Raghavendra MM, Lakshmaiah MV, Dastagiri S (2020) Image Enhancement using Histogram Equalization. *Test engineering management*, pp.11367–11370
29. Rajagopalan K, Babu S (2020) The detection of lung cancer using massive artificial neural network based on soft tissue technique. BMC Med Inform Decis Mak 20:282. https://doi.org/10.1186/s12911-020-01220-z
30. Rajakumar BR (2013) Impact of Static and Adaptive Mutation Techniques on Genetic Algorithm. Int J Hybrid Intell Syst 10(1):11–22. https://doi.org/10.3233/HIS-120161
31. Rajakumar BR (2013) Static and Adaptive Mutation Techniques for Genetic algorithm: A Systematic Comparative Analysis. Int J Comput Sci Eng 8(2):180–193. https://doi.org/10.1504/IJCSE.2013.053087
32. Rajakumar BR, George A (2012) A New Adaptive Mutation Technique for Genetic Algorithm. In: Proceedings of IEEE International Conference on Computational Intelligence and Computing Research (ICCIC), Coimbatore, India, pages: 1–7, December 18–20. https://doi.org/10.1109/ICCIC.2012.6510293
33. Rajeyyagari S (2020) Automatic speaker diarization using deep LSTM in audio lecturing of e-Khool Platform. J Netw Commun Syst 3(4):17–25
34. Ramana K, Kumar MR, Sreenivasulu K, Gadekallu TR, Bhatia S, Agarwal P, Idrees SM (2022) Early prediction of lung cancers using deep saliency capsule and pre-trained deep learning frameworks. Front Oncol 12:886739
35. Roy MRG (2020) Economic Dispatch Problem in Power System Using Hybrid PSO and Enhanced Bat Optimization Algorithm. J Comput Mech Power Syst Control (JCMPS) 3(3):27–33
36. Sadashiv Halbhavi B, Kodad SF, Ambekar SK, Manjunath D (2019) Enhanced Invasive Weed Optimization Algorithm with Chaos Theory for Weightage based Combined Economic Emission Dispatch. J Comput Mech Power Syst Control 2(3):19–27
37. Sarkar A (2020) Optimization Assisted Convolutional Neural Network for Facial Emotion Recognition. Multimed Res 3(2):35–41
38. Setio AAA, Traverso A, de Bel T, Berens MSN, Jacobs C (2017) Validation, comparison, and combination of algorithms for automatic detection of pulmonary nodules in computed tomography images: The LUNA16 challenge. Med Image Anal 42:1–13
39. Sharma H, Hazrati G, Bansal J (2019) Spider Monkey Optimization Algorithm. https://doi.org/10.1007/978-3-319-91341-4_4

40. Song L, Liu X, Chen S, Liu S, Liu X, Muhammad K, Bhattacharyya S (2022) A deep fuzzy model for diagnosis of COVID-19 from CT images. Appl Soft Comput 122:108883
41. Sundhari RPM (2021) Enhanced histogram equalization based nodule enhancement and neural network based detection for chest x-ray radiographs. J Ambient Intell Human Comput 12:3831–3839. https://doi.org/10.1007/s12652-020-01701-z
42. Swamy SM, Rajakumar BR, Valarmathi IR (Dec. 2013) Design of Hybrid Wind and Photovoltaic Power System using Opposition-based Genetic Algorithm with Cauchy Mutation, IET Chennai Fourth International Conference on Sustainable Energy and Intelligent Systems (SEISCON 2013), Chennai, India, https://doi.org/10.1049/ic.2013.0361
43. Tajbakhsh N, Suzuki K (2017) Comparing two classes of end-to-end machine-learning models in lung nodule detection and classification: MTANNs vs. CNNs. Pattern Recogn 63:476–486
44. Tiwari L, Raja R, Polat K (2020) Detection of lung nodule and cancer using novel Mask-3 FCM and TWEDLNN algorithms. Measurement 172:108882 (Cover date: February 2021)
45. Toğaçar M (2021) Disease type detection in lung and colon cancer images using the complement approach of inefficient sets. Comput Biol Med 137:104827 (Cover date: October 2021)
46. Toğaçar M, Ergen B, Cömert Z (2020) Detection of lung cancer on chest C.T. images using minimum redundancy maximum relevance feature selection method with convolutional neural networks. Biocybern Biomed Eng, In press, uncorrected proof, Available online 23 November 2019 40:23–39
47. Tremblay A, Taghizadeh N, MacGregor J-H, Armstrong G, Burrowes P (2019) Application of Lung-Screening Reporting and Data System Versus Pan-Canadian Early Detection of Lung Cancer Nodule Risk Calculation in the Alberta Lung Cancer Screening Study. J Am Coll Radiol 16(10):1425–1432
48. Venugopal VK, Vaidhya K, Murugavel M, Chunduru A, Mahajan H (2020) Unboxing A.I. - Radiological Insights Into a Deep Neural Network for Lung Nodule Characterization. Acad Radiol 27:88–95 In press, corrected proof, Available online 14 October 2019
49. Vijay R, Kumar A, Kumar A, Ashok Kumar VD, Rajeshkumar K, Ambeth Kumar VD, Saudagar AKJ, Abirami A (2021) COVIDPRO-NET: a prognostic tool to detect COVID 19 patients from lung X-ray and C.T. images using transfer learning and Q-deformed entropy, J Exp Theor Artif Intell. https://doi.org/10.1080/0952813X.2021.1949755
50. Wagh MB, Gomathi N (2019) Improved GWO-CS Algorithm-Based Optimal Routing Strategy in VANET. J Netw Commun Syst 2(1):34–42
51. Wanga T, Yang L (2020) Beetle Swarm Optimization Algorithm:Theory and Application, Neural and Evolutionary Computing, 8
52. Woźniak M, Połap D, Capizzi G, Sciuto GL, Frankiewicz K (2018) Small lung nodules detection based on local variance analysis and probabilistic neural network. Comput Methods Prog Biomed 161:173–180
53. Xie Y, Zhang J, Xia Y (2019) Semi-supervised adversarial model for benign–malignant lung nodule classification on chest C.T. Med Image Anal 57:237–248
54. Yin Y et al (2018) Tumor Cell Load and Heterogeneity Estimation From Diffusion-Weighted MRI Calibrated With Histological Data: an Example From Lung Cancer. IEEE Trans Med Imaging 37(1):35–46
55. Yin S, Li H, Liu D et al (2020) Active contour modal based on density-oriented BIRCH clustering method for medical image segmentation. Multimed Tools Appl 79:31049–31068. https://doi.org/10.1007/s11042-020-09640-9
56. Zhou X, Lin J, Zhang Z, Shao Z, Liu H (2020) Improved itracker combined with bidirectional long short-term memory for 3D gaze estimation using appearance cues. Neurocomputing 390:217–225 In press, corrected proof, Available online 20 October 2019